Sensors & Actuators: B. Chemical 291 (2019) 216–225

Contents lists available at ScienceDirect

Sensors and Actuators B: Chemical

journal homepage: www.elsevier.com/locate/snb

Highly sensitive sensors based on quasi-2D rGO/SnS_2 hybrid for rapid detection of NO_2 gas

Ming Cheng, Zepei Wu, Guannan Liu, Lianjing Zhao, Yuan Gao*, Bo Zhang, Fangmeng Liu, Xu Yan, Xishaung Liang, Peng Sun, Geyu Lu*

State Key Laboratory on Integrated Optoelectronics, Jilin Province Key Laboratory on Gas Sensors, College of Electronic Science and Engineering, Jilin University, Changchun, 130012, People's Republic of China

ARTICLE INFO

Keywords:
Gas sensor
SnS_2
Graphene
rGO
NO_2
2D materials

ABSTRACT

Nitrogen dioxide (NO_2) sensing is important in terms of the agriculture development and healthcare monitoring. However, relatively poor recovery kinetics at a low temperature is still a problem for NO_2 sensing and remains to be solved. In this work, we combine the excellent sensing properties and gas adsorption capacity of two- dimensional (2D) tin disulfide (SnS_2) hexagonal nanoflakes with the beneficial electrical properties of graphene to build high-performance NO_2 sensors by a simple and low-cost method. We found that the sensors based on the quasi-2D rGO-SnS_2 hybrids exhibited exclusive selectivity towards NO_2. The presence of rGO in hybrids decreased optimal working temperature effectively. Sensors based on 0.8% rGO-SnS_2 (G-SS) show almost an order of magnitude increase in response (32) compared to pristine SnS_2 (3.5). Especially, the response/recovery time is 50/48 s, respectively, demonstrating the favorable response/recovery kinetics of sensors. Such significant features can be attributed to the synergistic effect of the quasi-2D G-SS hybrid and the local heterojunctions in the interface between SnS_2 and rGO.

1. Introduction

Sensors as key devices acquire and transfer the external information, and play a crucial role in our life [1]. Among various sensors, gas sensors have attracted increasing attention, which can be applied in the environmental monitoring [2–4], individual healthcare [5,6] and production control [7,8]. In the multiple application scenarios, the detection and sensing of NO_2 is particularly important. NO_2 is a sort of quite common and important gas, which is mainly generated from the industrial production and daily life, such as, automobile exhaust, power station and fertilizer production. On the one hand, NO_2 seriously threat to human beings and plants. NO_2 is particularly harmful to human health at concentrations greater than 1 ppm, since it can paralyze the respiratory system thus lead to an overexposure [9]. NO_2 is also recognized as the origin of photochemical smog, since the ingredients of which are acid rain and ozone (O_3) that can be produced by NO_2 [10,11]. On the other hand, as reported, NO_2 can serve as a biomarker to reflect the human's physical condition in certain organs or tissues. For instance, the analysis reports of exhaled breath contribute to the diagnosing of lung tissues infections and gastrointestinal disorder symptoms [12,13]. In consideration of the significance of NO_2 detecting and the huge application potential of NO_2 gas sensors, it is essential to develop high-performance NO_2 sensing sensors, which can achieve the rapid real-time detection for NO_2 gas with an exclusive selectivity.

Recently, 2D materials have attracted extensive attention in sensing field due to its favorable physical and chemical properties. As the first generation of 2D materials, graphene consists of a single layer of carbon atoms, which form a honeycomb crystal structure by sp^2 hybridization [14]. Due to the high carrier mobility, decent chemical stability and high specific surface area, the researches about graphene in NO_2 sensing field have resulted in notable success [15,16]. However, so far, the reduced graphene oxide (an important derivative of graphene) is mainly utilized as a dopant to enhance the response and reduce the resistance of sensors, since the NO_2 sensors based on single rGO (reduced graphene oxide) are proved to possess a slow recovery kinetics and poor selectivity [17,18]. As the excellent properties of graphene come to light gradually, increasing interests have been spurred to inquire the graphene analogues and their composite nanostructures [19–21]. Transition metal dichalcogenide (TMDs), as new class of 2D materials, have been extensively applied in sensors field due to the unique thickness-dependent band gap and excellent electrochemical/thermal properties [22–24]. Because of the absence of dangling bonds

* Corresponding authors.
E-mail addresses: gaoyuan@jlu.edu.cn (Y. Gao), lugy@jlu.edu.cn (G. Lu).

https://doi.org/10.1016/j.snb.2019.04.074
Received 31 January 2019; Received in revised form 12 April 2019; Accepted 14 April 2019
Available online 15 April 2019
0925-4005/

in TMDs, the contact between TMDs and substrate of electrical device hardly affect the stability and mobility of materials. TMDs are proved to possess an excellent affinity to NO_2 gas molecule [25]. Upon exposure to NO_2, electron transfer will happen at the interface between NO_2 and sensing material surface according to the position of energy band and orbital hybridization of materials, resulting in a change in resistance [26,27]. Besides, the defects existed in TMDs is sulfur vacancies instead of oxygen vacancies, hence the TMDs-based sensors show more robust stability than metal oxide-based sensors, since the oxygen vacancies are considered as the origin of the long-term instability for metal oxide-based sensors [28,29].

Although tin is not a member of transition metal family, tin sulfide (SnS_2) exists in 2D planar crystalline structure similar to the TMDs and is widely investigated in sensors and other fileds due to its favorable properties presently [30,31]. The Sn atom layer is sandwiched between two layers of S atoms, and the adjacent layers of S atoms are connected by weak Vanderwaals. In addition, the energy gap of band structure for SnS_2 is inclined to be regulated by temperature, which can be utilized to enhance the recovery kinetics by raising the temperature appropriately [32,33]. More importantly, the adsorption between NO_2 and SnS_2 is proved to be a physisorption, which relies on the intermolecular forces, namely Vanderwaals. The activation-energy for physisorption is far less than that needed for chemisorption. In addition, physisorption of gas molecule can occur at low temperature [34]. Despite the aforementioned merits, the outcomes are still far from the expectation and encounter several bottlenecks in the practical application. Firstly, the pristine SnS_2 yields a weak response towards NO_2. Secondly, the resistance of SnS_2 in air tends to be large at a low temperature, however, once increasing the temperature, the SnS_2 faces with risks of oxiding to SnO_2.

In view of the above analysis on the NO_2 sensing performance, whether SnS_2 or rGO, the development in isolation can't lead to satisfactory results, which inspires us to employ hybrids containing the above two materials to enhance the NO_2 sensing performance by the integration of their advantages. In addition, the 2D/2D rGO-SnS_2 (quasi-2D G-SS) heterostructures possess advantages of abundant coupling interfaces and large contact surface, which would produce more active site and enhance the sensing performance.

In this work, we fabricated a quasi-2D G-SS hybrid in a simple and mild method, the NO_2 sensing performance was optimized by regulating the content of rGO in samples. The optimized sensors show excellent sensing properties, such as enhanced sensing response, lowered optimal working temperature and rapid recovery. Especially recovery kinetics is adaptive to the fast proceeding speed for treating mass information in the big-data era. In brief, the market-oriented NO_2 sensors exploited in our work has a promising prospect in the field of environmental monitor and healthcare practical application.

2. Materials and methods

2.1. Synthesis of SnS_2 powder

The SnS_2 powder was synthesized beginning from the reagents obtained from Sinopharm Chemical Reagent Co., Ltd (Shanghai, China). First, 5.7 mmol of tin chloride pentahydrate ($SnCl_4{\cdot}5H_2O$, ≥99%) was dissolved in a breaker with 50 ml of DI water (deionized water). After continuous stirring of 10 min, the homogeneous solution of Sn^{4+} was obtained. Then, 22.9 mmol of thiourea (NH_2CSNH_2, ≥99%) and 31.5 ml of DI water were added to the solution. In this process, S^{2-} ions were produced by reaction [35,36]. Under stirring for 30 min, the resulting solution was transferred in a 100 ml Teflon-lined autoclave and then put in an oven, the temperature of which preset at 180 °C. After hydrothermal reaction for 24 h and cooling to room temperature, the SnS_2 nanoflakes were collected by centrifuging and washing with ethanol and DI water several times.

2.2. Synthesis of G-SS compound

The rGO was synthesized starting from graphite powder by a modified Hummers method [37]. For the synthesis of G-SS compound, first, 0.1 g of SnS_2 powder and 40 ml of DI water were added to a breaker under stirring to form homogenous solution. Then the above solution was treated by water bath at 80 °C with magnetic stirring for 6 h, in the process of which, 0.2 ml of GO solution (3 mg/mL) was added drop by drop. After cooling to room temperature, the precipitate was collected and marked as 0.6% G-SS. Similarly, with other experimental conditions unchanged the compound containing 0.26 ml, 0.33 ml, 0.45 ml, 0.63 ml, and 0.83 ml GO solution were synthesized and marked as 0.8% G-SS, 1.0% G-SS, 1.36% G-SS, 1.9% G-SS, 2.5% G-SS throughout the entire article.

2.3. Characterization

Both the SnS_2 and G-SS samples were analyzed by X-ray powder diffraction (XRD), with a Rigaku D/max-2550 X-ray diffractometer with high-intensity Cu Kα radiation (λ = 0.154 nm) in the range of 10–80° (2θ). The field emission scanning electron microscopy (FESEM) images were obtained on a JEOL JSM-7500 F microscope operating at 15 kV. Transmission electron microscopy (TEM), high-resolution transmission electron microscopy (HRTEM) and EDS mapping were obtained on a JEOL JEM-2100 F microscope with accelerating voltage of 200 kV. Raman spectroscopy analyses were conducted on a RENISHAW INVIA Micro-Raman spectrometer. The X-ray photoelectron spectroscopy (XPS) data were recorded on a PREVAC XPS system. The specific surface area was estimated by the Brunauer–Emmett–Teller (BET) equation based on the nitrogen adsorption isotherm, which was measured with a Micromeritics Gemini VII apparatus. Thermogravimetric analysis (TGA) was performed using a Thermogravimetric Analyzer (Netzsch STA 499 F3).

2.4. Sensor fabrication and performance test

The process of sensor fabrication was as followed and showed in Fig. S1. First, a moderate amount of samples and DI water were added to reagent bottle with small capacity, after an ultrasound treatment for a while, a thick paste was obtained. Then, the paste was coated compactly on a ceramic tube, on which a pair of gold electrode was preinstalled acting as the sensing film. Then, a Ni-Cr alloy coil was inserted into the ceramic tube entirely to control the temperature precisely. Finally, the ceramic tube was welded onto the sensor base and aged at 200 °C for 48 h.

The electrical resistance of both SnS_2 and G-SS were measured by static testing method and recorded by a data-acquiring system at 20% relative humidity. First the sensors were put in a bottle filled with air for several hours at working temperature until the electrical resistance reach stability. The working temperature ranged from 25 °C to 240 °C. Then a certain concentration tested gas was injected to the bottle. After the resistance became steady, the sensor was transferred to a bottle filled with air to recover. For N-P compound, the conduction type was likely to change once the mass ratio of N/P reached the threshold. The sensitivity was defined as R_g/R_a (when $R_g > R_a$) and R_a/R_g (when $R_a > R_a$), where R_a and R_g were the resistance of sensors in air and NO_2 gas, respectively.

3. Results and discussion

3.1. Material characterization

XRD was conducted to investigate the crystal structure of as-synthesized samples. The results of measurement were shown in Fig. 1. According to the phase matching, the SnS_2 material was in single phase and the peaks were all in accordance with the Berndtite-2H, a

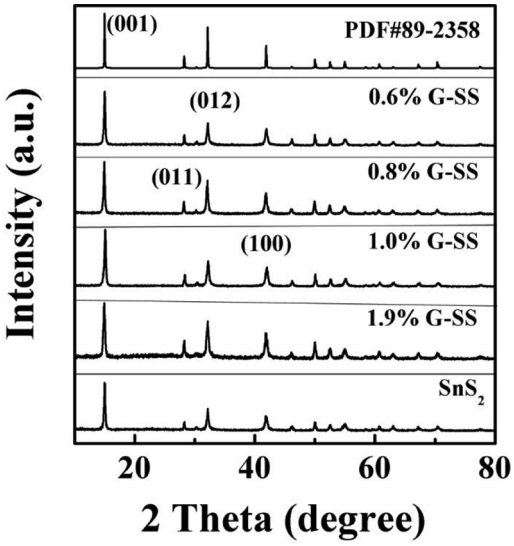

Fig. 1. XRD patterns of SnS_2 and G-SS samples.

Table 1
Crystallite size and specific surface area of SnS_2 and G-SS samples.

Samples	Crysllite size (nm)
SnS_2	116
0.6% G-SS	121
0.8% G-SS	120
1.0% G-SS	120
1.9% G-SS	121

hexagonal cell structure with Space Group P-3m1. Notably, the peaks intensity and position of SnS_2 remain unchanged after the introduction of rGO, indicating the procedure and the material in experiment caused no damages the crystallinity of SnS_2. In addition, no peaks belonging to the rGO appeared, this may be due to the low amount of rGO. Besides, crystallite sizes were calculated by Scherrer equation, $D = 0.8\lambda/\beta\cos\theta$, where D was the crystallite size, λ was the wavelength of X-ray radiation, β was the full width at half-maximum intensity (fwhm in radians), θ was diffraction angle. The average crystallite sizes of samples were listed in Table 1. Compared to the pristine SnS_2, the grain size of G-SS samples increased, which could be attributed to the grain regrowth in the process of water bath. Notably, Fig. S2 showed the XRD pattern of SnS_2 and 0.8% G-SS samples after aging at 200 °C for 96 h, the results of which turned out that the crystal structure remained unchanged.

The morphologies and other geometrical parameters were measured by FESEM and AFM. Fig. 2 (a) displayed the FESEM image of SnS_2, it was easy to notice the presence of hexagonal nanoflakes ranging from 200 nm to 1 μm. The AFM analysis, (see in Fig. S3), proved that the nanoflakes in FESEM image were about 10 nm thick, which was tens of monolayers of SnS_2 (the thickness of a monolayer was about 0.59 nm) [38]. From the FESEM image of 0.8% G-SS (Fig. 2 (b)), it was clearly noticed that numerous SnS_2 nanoflakes adhered to the wrinkled rGO sheets, which was more apparent in FESEM image at high magnification, as shown in Fig. 2 (c). In comparison to the pristine SnS_2 nanoflakes, the hexagon edge of 0.8% G-SS suffered slight damages and appeared zigzag, this may be caused by the crash among the nanoflakes during the stirring procedure with water bathing. Notably, Fig. S4 showed the SEM image of SnS_2 and 0.8% G-SS samples after aging at 200 °C for 96 h, the results of which turned out that the morphology remained unchanged.

TEM was then employed to give a further insight into the material. Fig. 2 (d) displayed the TEM image of 0.8% G-SS at low magnification. As one can see, only several intact SnS_2 nanoflakes could be clearly identified, the majority of nanoflakes severely adhered to the rGO sheets leading to a large area of shadow, which interfered the observation of rGO beyond doubt. To confirm the presence of rGO, EDS mapping was conducted, results of which were shown in Fig. 3. The analysis showed the presence of S, Sn and C element which all distributed where the samples existed. Undoubtly, S and Sn element derived from the SnS_2 nanoflakes. The C element could be attributed to the skeleton of rGO, which proved the presence of rGO in the compound rigorously.

The HRTEM analysis (Fig. 3 (e–f)) revealed crystallographic parameter of 0.8% G-SS, which matched well with the results of XRD measurement. The fringe spacing of 0.590 nm and 0.315 nm could be discerned distinctly in the inset of upper right corner of Fig. 3 (f), which accorded with the (001) and (100) lattice plane of hexagonal SnS_2. Similarly, the fringe spacing of 0.279 nm was in accordance with the (011) lattice plane of SnS_2. In addition, the curving lattice fringes where around the edge of SnS_2 grains (see in the rectangle area selected with dotted line in the Fig. 3 (e–f)) were an equally strong evidence of the presence of rGO.

The Raman spectrum of 0.8% rGO-SnS_2 (see in Fig. 4 (a)) displayed three peaks at ~314 cm^{-1}, ~1340 cm^{-1} and ~1582 cm^{-1}, respectively. The peak at ~314 cm^{-1} could be attributed to the out-of-plane vibrational mode (A_{1g}) of 2H SnS_2, which was in accordance with the XRD results. [39] Another peak corresponding to the in-plane Sn−S bonds vibrational mode (E_g) for SnS_2, was not be observed, which may be due to the damping of scattering centers in plane caused by the nano size of SnS_2. [40,41] The latter two peaks resulted from the well-defined D and G bands of carbon-based material, respectively. It was widely believed that the G band, a characteristic peak, could be applied in the determination of graphite degree for carbon-based material, since the G band resulted from the E_{2g} phonon of sp^2 hybridizatio of atom. From the measurement it was remarkably observed that the peaks position of G band (1582 cm^{-1} for 0.8% G-SS) blue-shifted in comparison with GO (1591 cm^{-1}), an indication of restoring of graphene sp^2 system structure during the experiment, which was a strong proof that the GO was reduced to rGO. In addition, the ratio of I_D/I_G was regarded as an important index to assess the disorder degree of carbon-based material. The above value increased from 0.91 (for GO) to 1.13 (for 0.8% G-SS), which was also presumably due to the generation of new graphene flakes during the stirring. From the nitrogen adsorption-desorption analyses, (see in Fig. 4 (b–c)), the specific surface area was calculated to be 5 m^2/g and 12 m^2/g for SnS_2 and 0.8% G-SS based on the BET theory, which could be attributed to the introduction of 2D rGO. TGA analyses were conducted to probe into the thermal stability of as-prepared samples. Notably, we only conducted TG measurements on pristine SnS_2 and 0.8% rGO-SnS_2 for the following reasons. On the one hand, when working temperature of sensors ranged from room temperature to 220 °C, whether SnS_2 or rGO could remain chemical stable on the basis of our previous study, thus TG measurements were conducted according to final sensing properties to confirm further the reliability of our data. On the other hand, the temperature that SnS_2 and rGO began to decompose wouldn't vary drastically with the adding amount of rGO, therefore, we only conduct TG measurements on pristine SnS_2 and 0.8% rGO-SnS_2. The results were reported in Fig. 4 (d).A weight loss happened on both SnS_2 and 0.8% G-SS at the initial stage, which may be due to the absorbed water and moister. It was remarkably noticed that a weight loss started from 380 °C until 600 °C, which could derive from the evaporation of the residual organic reagents and rGO in the samples. At temperature exceeding 620 °C, SnS_2 started to oxide to SnO_2. As a consequence of TG measurement, it derived that the as-prepared samples can maintain strong chemical stability at temperature below 380 °C.

Then X-ray photo-electron spectroscopy (XPS) was employed to confirm the element composition and chemical configuration. The

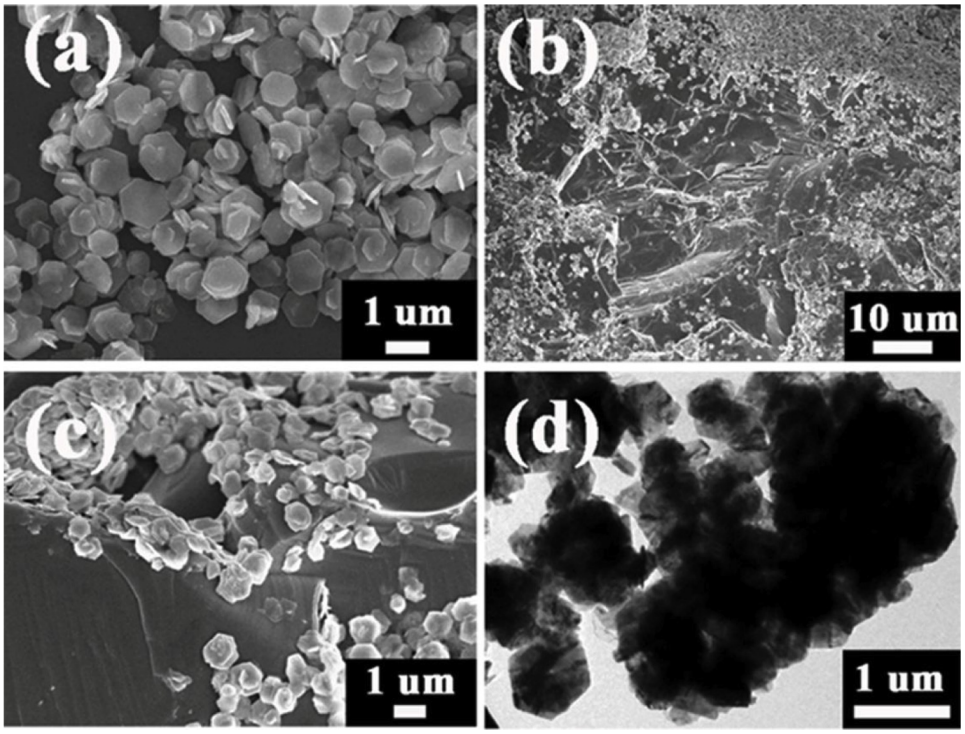

Fig. 2. SEM image of SnS_2 samples (a) and 0.8% G-SS (b–c); TEM image of 0.8% G-SS (d).

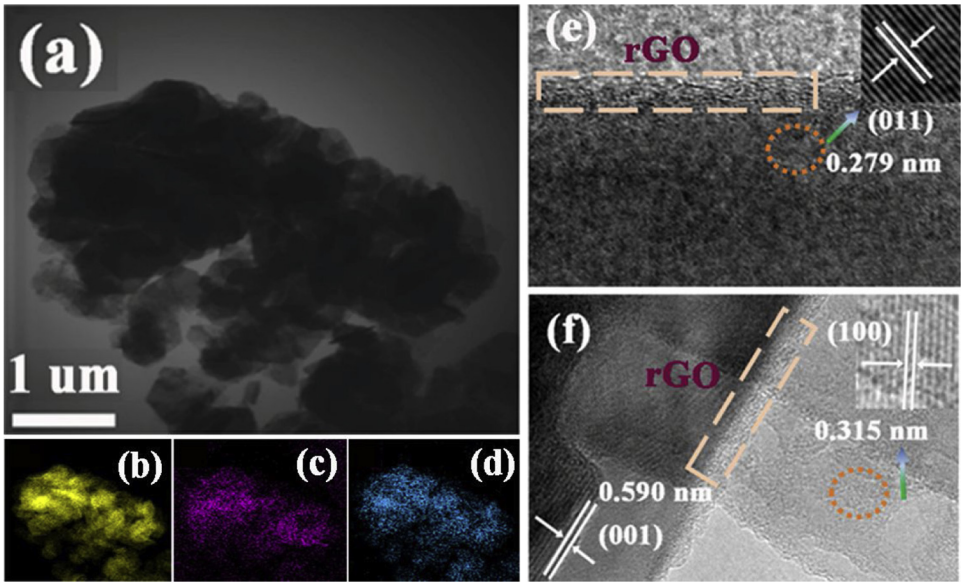

Fig. 3. STEM image of 0.8% G-SS (a) and its element mapping image of S, C, Sn (b–d, respectively); HRTEM image of 0.8% G-SS (e–f).

survey scan spectrum of both SnS_2 and G-SS (see in Fig. 5 (a)) showed the presence of C, S and Sn element with no other impurity peaks detected. S and Sn element derived from the SnS_2, and C element could be attributed to the presence of graphene or contaminated carbon for equipment correction. The results accorded with the elementary composition of G-SS, meaning the purity of as-prepared material. The high-resolution S 2p XPS spectra in Fig. 5 (b) displayed the peaks at 161.86 eV and 162.85 eV analogous to S $2p_{3/2}$ and S $2p_{1/2}$ for SnS_2 respectively [42]. However, the position of above peaks decreased to 161.68 eV and 162.78 eV for G-SS samples. The same phenomenon happened to the Sn 3d XPS spectra (see in Fig. 5 (c)), the Sn $3d_{5/2}$ and Sn $3d_{3/2}$ located at 486.69 eV and 495.15 eV for SnS_2, however, the corresponding peaks position of G-SS shifted to 486.61 eV and 495.06 eV respectively [43]. The peaks moving in the direction of lower energy caused by the electron transferred from the rGO indicated the strong interaction between rGO and SnS_2, a proof of construction of heterojunctions in the interface of SnS_2 and rGO. The C 1 s spectra showed peaks at 284.5 eV, 286.4 eV and 288.5 eV, which corresponded to the C═C, C—O and C—S bonds (see in Fig. 5 (d)) [44–46]. Notably, the C—S bonds could cause the S vacancy in the SnS_2 [47]. It was proved easier for the remaining electron in S vacancy to be excited to the conduction band.

3.2. Sensors performance tests

We first analyzed the response-temperature functione of sensors,

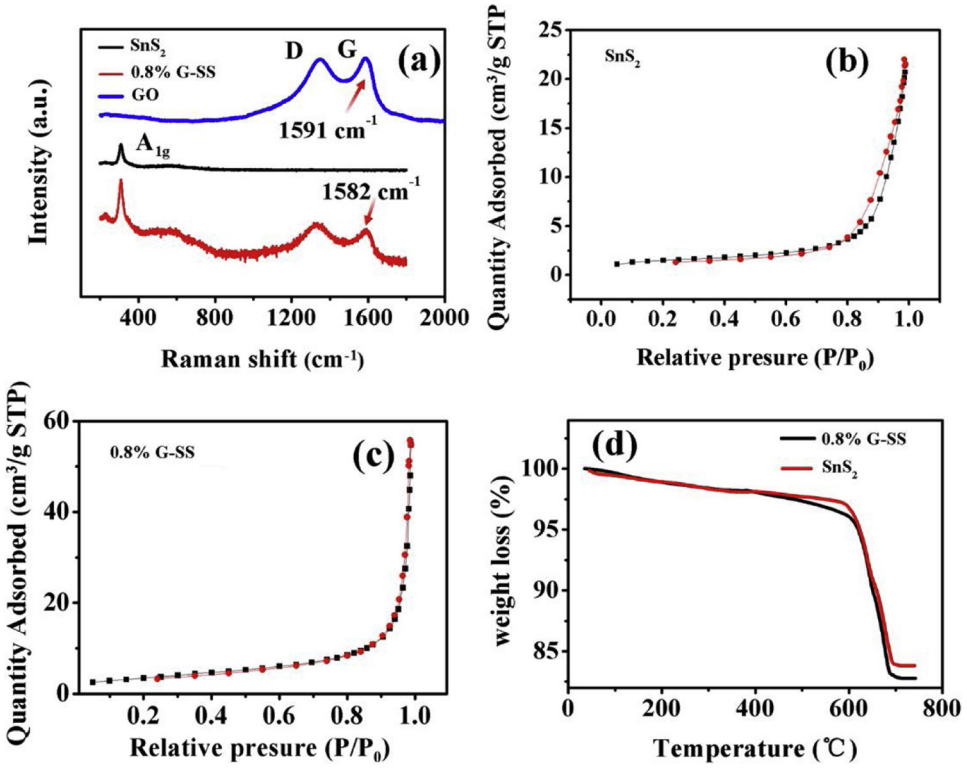

Fig. 4. Raman spectrum for SnS_2, 0.8% G-SS and GO (a); The nitrogen adsorption-desorption isotherms of SnS_2 and 0.8% G-SS (b–c); TGA curves measured on the SnS_2 and 0.8% G-SS (d).

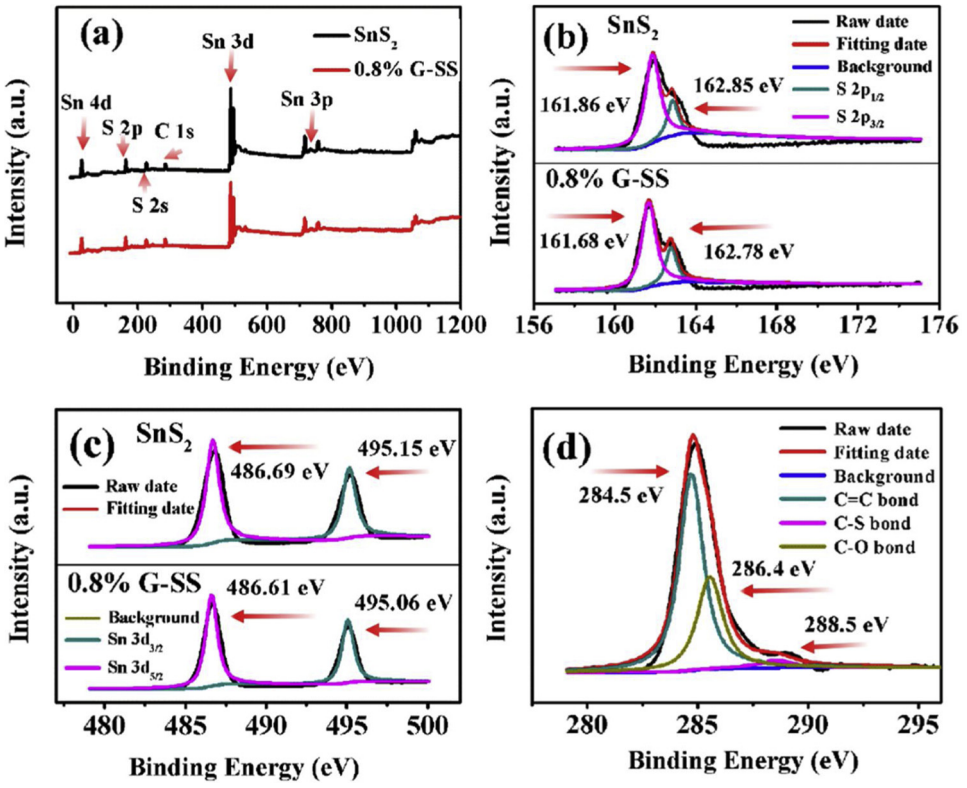

Fig. 5. XPS spectrum of SnS_2 and 0.8% G-SS. XPS survey (a); High-resolution XPS spectra of S 2p, Sn 3d and C1 s (b–d).

since the tempetature not only represented the amount of enengy consumption, but also impacted the equilibrium of gas adsorption and disorption on the surface of material as well as the position of energy bands, which played a critical role in response magnitude and kinetics. Results of tests for sensors based on the SnS_2 and G-SS were shown in Fig. 6 (a). As displayed, peaks could be readily discerned for sensors based on the SnS_2, 0.6%, 0.8% and 1.0% G-SS, which was a consequence of competition between gas adsorption and disorption. In

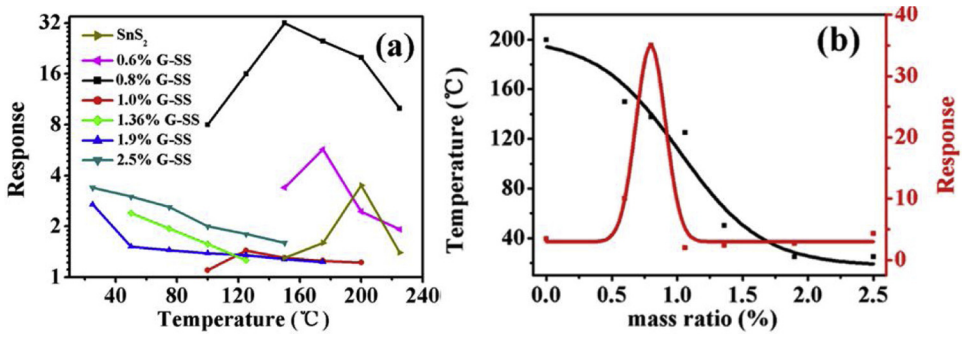

Fig. 6. Response of sensors based on the SnS_2 and G-SS to 5 ppm NO_2 as a function of operating temperature (a); Response and optimun temperature of sensors to 5 ppm NO_2 (b).

contrast, no peaks just a downward trend were noticed for sensors based on 1.36%, 1.9% and 2.5% G-SS, which meant RT was optimum operating temperature in the measurable range. Next we investigated the effct of rGO amount on sensing response more intuitively (see in Fig. 6 (b)). As the mass ratio of rGO increased, the optimum operating temperature decreased gradually until to RT, which could be interpretted this way that the rGO boosted the adsorption of gas and lower the activation energy of SnS_2 surface. For sensors based on 0.8% G-SS, the optimum temperature decreased from 200 °C for SnS_2 to 150 °C. On the other hand, as the mass ratio of rGO ranged from 0% to 1.0%, the response of sensors to 5 ppm NO_2 rose initially and decreased subsequantly, which was a consequence of competition between SnS_2 and rGO. As the mass ratio of rGO exceed 1.0%, the response increased gradually, meaning the1.0% was the threshold of transition between N/P conduction type, which caused a minimum response. It could be found that, in coparison with pristine SnS_2, the 0.8% G-SS sensed NO_2 strongly, with an increase in response to 5 ppm NO_2 nearly one orders of magnitude (from 3.5 to 32).

Then, measurments were conducted to analyze the selectivity of as-prepared sensors, and the results were reported in Fig. 7. As one can see, whether the rGO was introduced or not, the sensors sensed NO_2 selectively, as the responses to other tested gases were negligible. In addition, the sensors yielded a weak response (less than 2) towards sulfur dioxide and hydrogen sulfide, which could ascribe to the affinity interaction between S vacancy and sulfur-containing gas.

The dynamic response of sensors based on the SnS_2 and G-SS to NO_2 at a series of concentrations was illustrated in Fig. 8 (a) and Fig. S5. As seen, as the NO_2 concetration increased, the response of sensors all gradually rose with the exception of 1.0% rGO-SnS_2。 The response of 1.0% rGO-SnS_2 hardly rose and maintained at around 1, which could be atributed to the sharp decline of carrier concentration before transition of conduction type. The analysis on the correlation between NO_2 concetration and response (see in Fig. 8 (b)), evidenced that the sensors based on the 0.8% G-SS possessed a larger NO_2 detection range, since there was no sign that the reponse to NO_2 was on the threshold of saturation. In the meantime, the sensors based on the 0.8% G-SS possessed a lower detection limit (500 ppb). In order to compare the resistance of sensors in air and the response and recovery kinetics of sensors more intuisively, response curves of sensors towards 5 ppm NO_2 at their respective optimum temperature were put together in Fig. 9 (a). As shown, a N-type response to NO_2 was observed for sensors based on the SnS_2, 0.6%, 0.8% and 1.0% G-SS. In contrast, a P-type response was observed for sensors based on 2.5% G-SS. As was known, SnS_2 and rGO belonged to N-type and P-type semiconductor, respectively. When trace of rGO was introduced to the SnS_2, it acted as dopants thus the material ramained a N-type semiconductor. However, as the amount of rGO continued to increase and reached the threshold, the rGO became the dominant agent thus the material transformed into a P-type semiconductor. It was remarkable to notice that the resistance in air of sensors varied widely and a downward trend could be roughly observed as the amount of rGO increased (inset of Fig. 9 (a)). The resistance in air was 40, 95, 16, 2.6, 5.5 and 1.75 MΩ for sensors based on the SnS_2, 0.6%, 0.8%, 1.0%, 1.9% and 2.5% G-SS at their optimal operating temperature, respectivly. Obviously, expection have been achieved that the reduction of resistance along with the decline of operating temperature. For 0.8% G-SS, the resistance droped from 40 MΩ at 200 °C (pristine SnS_2) to16 MΩ at 150 °C, considering the strong temperature dependence of band structure of SnS_2, it was a substantial improvement. As a consequense of the above temperature and resistance test, it derived that operating temperature and resistance of SnS_2-based sensors could be lowered dramatically by adjusting rGO content, which opened its use in pratical production.

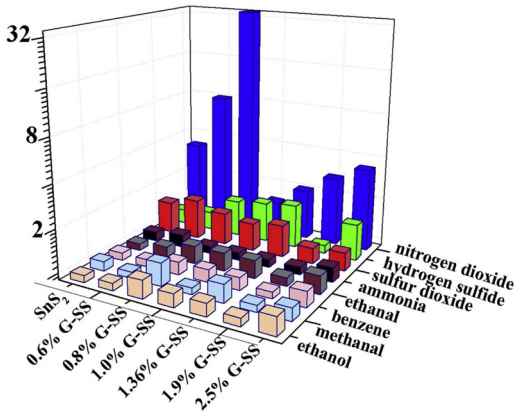

Fig. 7. Response of sensors based on the SnS_2 and G-SS to 5 ppm gases (NO_2, SO_2, NO_2, NH_3 and so on) at their respective optimum temperature.

Response/recovery time was a general evaluation criterion for response/recovery kinetics. According to the response curves of sensors, the response/recovery kinetics could be regulated effectively by the addition of appropriate amount of rGO. On the one hand, owing to the high carrier mobility of rGO, the addition of rGO could boost the electron transfer between SnS_2 surface and NO_2; on the other hand, the recovery kinetics of pristine rGO for NO_2 has been proved to be poor, which usually be unable to recovery to original baseline. Given this, an investigation was conducted to ascertain the optimum addition amount of rGO for rapid NO_2 detection and recovery, and the results were reported in Fig. 9 (b). As shown, the response time and recovery time displayed a generally consistent trend. For sensors based on the 0.6% G-SS, the response/recovery time both rose by several time. However, as the amount of rGO increased to 0.8%, the response/recovery time declined a little bit instead, from 60 s/60 s for pristine SnS_2 to 50 s/48 s. Then as the amount of rGO kept rising, the response/recovery time increased along. This could be explained this way as followed. When the amout of rGO was tiny, the SnS_2 nanoflakes aggregated and adhered onto the rGO seriously, which exerted severe impact on gas diffusion and thus hindered the response/recovery kinetics. As the amount of

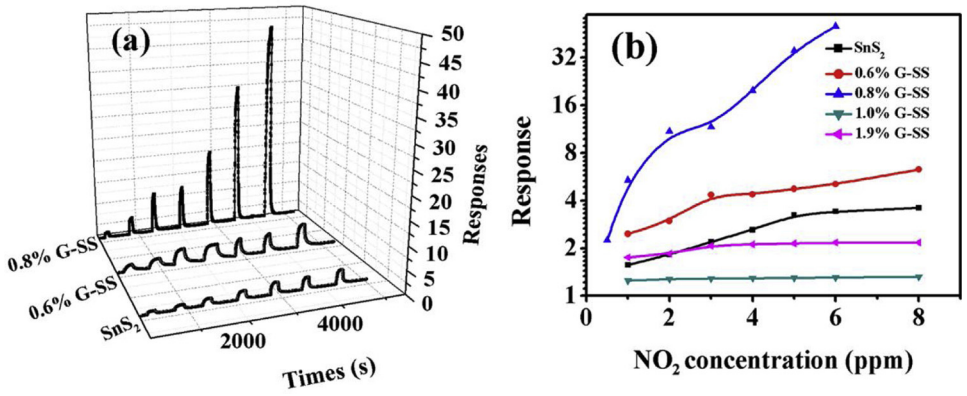

Fig. 8. Dynamic response curves of sensors based on the SnS_2 and G-SS towards NO_2 gas at concentration ranging from 500 ppb to 8 ppm at their respective optimum temperature (a); Response curves of sensors towards 5 ppm NO_2 at their respective optimum temperature (b).

rGO reached to threshold, namely 0.8% in this work, the high carrier mobility of rGO became the dominant effect and offset the disadvantages of agglomeration, thus the response/recovery time both dropped. As the amount of rGO continued to increased, the rGO gradually replaced the SnS_2 and acted as the dominent sensing material, presenting a poor kinetics. It was remakable to notice that when the amout of rGO rose beyond 1.0%, the recovery time fell in the range from 10 min to 15 min, a too large value to applied in pratical use. The comparison of sensing perforamnce among SnS_2 and G-SS was listed in Table 2. As a consequense of above response magnitude and response/recovery kinetics measurements, it derived that the optimum addition amount of rGO fell at 0.8%.

Next, results of the tests for sensors based on SnS_2 and 0.8% G-SS in wet condition (ranging from 20% RH to 90% RH) were shown in Fig. S6. As shown, the response of the sensors based on SnS_2 (black curve) dropped by 35% as the RH increased from 20% to 90%, however, 91% of entire decline happened in the range from 20% to 40%, which meant the impact of humidity on response achieved saturation as the RH rose beyond the 40%. In contrast, the response of sensors based on 0.8% G-SS dropped by 55% throughout. However, only a slight change was noticed in the range from 20% to 40%, manifesting the sensors based on 0.8% G-SS was qualified for task in low-RH environment.

In order to verify the reproducibility and continuous availability of sensors based on the 0.8% G-SS in practical use, the sensors was tested by transferring them from air to NO_2 and from NO_2 to air for 4 times continuously, and the results was reported in Fig. 10. (black curve). As shown, the reproducibility of NO_2 sensing was ralatively acceptable, the fluctuation may be due to the experiment error. Furthermore, the long-term stability analyse in Fig. 10 (red curve), evidenced that the sensors based on the 0.8% G-SS was robust, since the fluctuation of response to 5 ppm NO_2 was within the acceptable margin of error.

An objective comparison was made to evaluate the advancement of

Table 2
Comparison of sensing performance among SnS_2 and G-SS samples.

Samples	Response	Working temperature (°C)	Res-rec time[1] (s)
SnS_2	3.5	200	60/60
0.6% G-SS	5.7	175	100/200
0.8% G-SS	32	150	50/48
1.0% G-SS	1.44	125	70/80
1.36% G-SS	2.4	50	120/800
1.9% G-SS	2.7	25	157/1186
2.5% G-SS	3.39	25	380/4600

[1] res/rec time, response/recovery time.

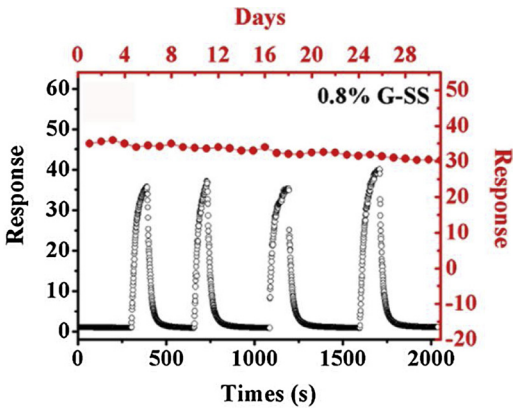

Fig. 10. Reproducibility and long-term stability of sensors based on the 0.8% G-SS at 150 °C.

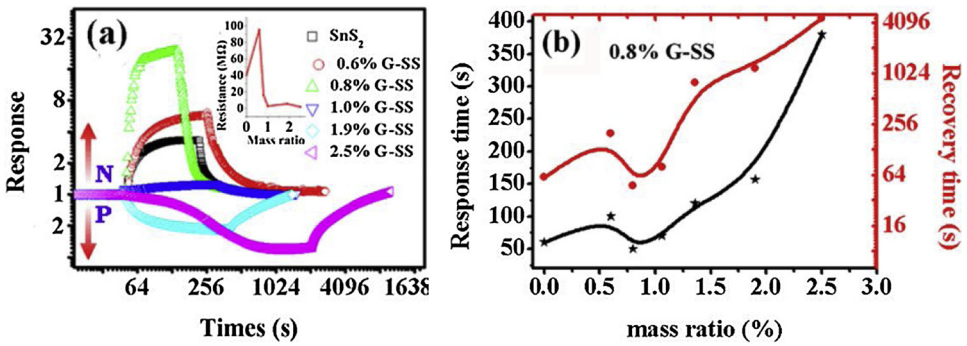

Fig. 9. Response curves of sensors towards 5 ppm NO_2 at their respective optimum temperature and the function of sensor resistance in air visus mass ratio of rGO (inset of Fig. 9) (a); Response and recovery time of sensors to 5 ppm NO_2 gas as a function of mass ration of rGO (b).

Table 3
A comparison in sensing performance of sensors based on the reported literatures and our work.

Sensing material	Working temperature (°C)	Sensing Concentration (ppm)	Properties Response	Res/rec time[1] (s)	Ref.
SnS_2	120	10	36.33	170/140	[34]
MoS_2	100	100	21.56%	71/310	[48]
ZnO	300	2.42	4.3%	180/360	[49]
rGO	RT[2]	10	5.39	1000/3000	[50]
MoS_2-rGO	150	5	8%	/	[51]
WS_2/graphene	180	2	4%	/	[52]
ZnO/rGO	RT	0.1	4.7%	90/150	[53]
SnS_2/SnO_2	80	8	5.3	159/279	[54]
rGO-SnS_2	150	5	32	50/48	Present wok

[1] res/rec time, response/recovery time.
[2] RT, room temperature.

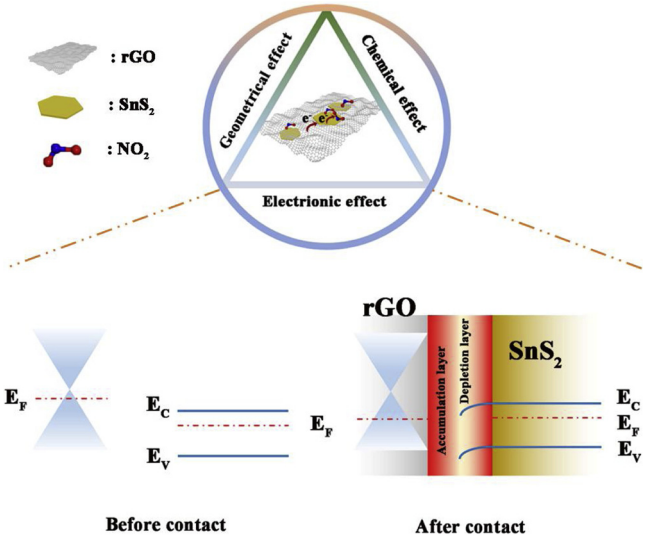

Fig. 11. Schematic diagram of the sensing mechanism for the enhanced gas response to NO_2.

our work, and the results were reported in Table 3. In contrast, the sensors based on the 0.8% G-SS showed near-perpect performance without obvious shoutcoming. While achieving quick response/recovery kinetics, the sensors possessed an excellent response magnitude. Given above merits, the sensors based on combining SnS_2 and rGO offered a possibility to achieve real-time detecting of NO_2, and could be exploited in industrial production and health-oriented applications.

Gas sensing was a process of electron transfer between gas molecules and sensing materials. Upon exposure to NO_2 gas, NO_2 would trap electron from conduction band of SnS_2 and then yield an increase in resistance of sensing materials. Compared to pristine SnS_2, the enhancement in NO_2 sensing properties after the introduction of rGO could be attributed to following three aspects (as shown in Fig. 11): 1) the geometrical effects caused by the construction of quasi-2D hybrid; 2) electronic sensitive effect resulted from the heterojunction between the interface of SnS_2 and rGO; 3) chemical sensitive effect stemmed from the S vacancy on the surface of SnS_2. Firstly, the 2D/2D heterostructures of SnS_2 and rGO possessed large specific surface area, which increased the electronic transmission path and active centers for NO_2 adsorption. In addition, the introduction of rGO could alleviate the stack and agglomerate of SnS_2, which contributed to the diffusion and adsorption of gas molecules. Secondly, as the work function of SnS_2 (5.09 eV) was higher than rGO (2.5 eV), a heterojunction would come into being once SnS_2 ohmic-contact with rGO. The electron would transfer from rGO to SnS_2 until Fermi level reach equilibrium, leading to an electron accumulation layer in SnS_2 and hole accumulation layer in rGO, which could be regulated via NO_2 adsorption and desorption and provide addition active sites. Notably, the inherent 2D structures of SnS_2 and rGO allowed a compact and extensive contact with each other, which increased the junction area. In addition, the build-in electric field could accelerate the electron transfer between NO_2 and sensing materials and benefit the NO_2 adsorption. Finally, S vacancy was proved to be an efficient active center for NO_2 adsorption and acted as electron transfer bridge. In conclusion, the sensors based on the quasi-2D G-SS showed excellent NO_2 sensing properties by the synergistic effects of the hybridization.

4. Conclusion

In this work, we successfully developed a novel NO_2 sensors based on quasi-2D G-SS hybrid by a simple and low-cost method. The addition amount of rGO was investigated thoroughly and the optimum mass ratio of rGO was determined as 0.8%. Compared with pristine SnS_2, the sensors based on 0.8% G-SS yielded an excellent response (32) towards 5 ppm NO_2 gas, an increase nearly one order of magnitude. In the meantime, the sensors showed exclusive selectivity towards NO_2 and robust long-term stability. The enhancement in NO_2 sensing properties could be attributed to the synergistic effects of the hybridization. We hoped the market-oriented NO_2 sensors in our work could advance the progress of sensors based on quasi-2D materials and extensively applied in the field of environmental monitor and healthcare practical production.

Acknowledgments

This work was supported by grants from the National Nature Science Foundation of China (61304242, 61520106003), Program for Chang Jiang Scholars and Innovative Research Team in University (IRT_17R47), and National High-Tech Research and Development Program of China (863 Program, No. 2014AA06A505). Application and Basic Research of Jilin Province (20130102010JC), STIRT-JLU (2017TD-07).

Appendix A. Supplementary data

Supplementary material related to this article can be found, in the online version, at doi:https://doi.org/10.1016/j.snb.2019.04.074.

References

[1] M. Swan, Sensor mania! The internet of things, wearable computing, objective metrics, and the quantified self 2.0, J. Sens. Actuator Netw. 1 (2012) 217–253.
[2] W.W. Walters, M.G. Hastings, Collection of ammonia for high time-resolved nitrogen isotopic characterization utilizing an acid-coated honeycomb denuder, Anal. Chem. 90 (2018) 8051–8057.
[3] J.J. Chai, M.G. Hastings, Collection method for isotopic analysis of gaseous nitrous acid, Anal. Chem. 90 (2018) 830–838.
[4] L. Fibiger, M.G. Dorothy, Hastings, First measurements of the nitrogen isotopic composition of NO_X from biomass burning, Environ. Sci. Technol. 50 (2016) 11569–11574.
[5] P.J. Chien, T. Suzuki, Biochemical gas Sensors (Biosniffers) using forward and

reverse reactions of secondary alcohol dehydrogenase for breath isopropanol and acetone as potential volatile biomarkers of diabetes mellitus, Anal. Chem. 89 (2017) 12261–12268.
[6] K. Iitani, T. Sato, Fluorometric sniff-cam (gas-imaging system) utilizing alcohol dehydrogenase for imaging concentration distribution of acetaldehyde in breath and transdermal vapor after drinking, Anal. Chem. 90 (2018) 2678–2685.
[7] V.L. Patil, S.A. Vanalaker, Fabrication of nanostructured ZnO thin films based NO_2 gas sensor via SILAR technique, Sens. Actuators B Chem. 239 (2017) 1185–1193.
[8] S. Brenet, A. John-Herpin, Highly-selective optoelectronic nose based on surface plasmon resonance imaging for sensing volatile organic compounds, Anal. Chem. 90 (2018) 9879–9887.
[9] M. Guarnieri, J.R. Balmes, Outdoor air pollution and asthma, Lancet 383 (2014) 1581–1592.
[10] A. Tamvakos, K. Korir, D. Tamvakos, NO_2 gas sensing mechanism of ZnO thin-film transducers: physical experiment and theoretical correlation study, ACS Sens. 1 (2016) 406–412.
[11] R. Atkinson, Atmospheric chemistry of VOCs and NOx, Atmos. Environ. 34 (2000) 2063–2101.
[12] J.L. Puckett, S.C. George, Partitioned exhaled nitric oxide to non-invasively assess asthma, Resp. Physiol. Neurobiol. 163 (2008) 166–177.
[13] J.Z. Ou, C.K. Yao, A. Rotbart, Human intestinal gas measurement systems: in vitro fermentation and gas capsules, Trend. Biotechnol. 33 (2015) 208–213.
[14] B. Zhang, M. Cheng, Room temperature NO_2 gas sensor based on porous Co_3O_4 slices/reduced graphene oxide hybrid, Sens. Actuators B Chem. 263 (2018) 387–399.
[15] B. Zhang, G.N. Liu, The preparation of reduced graphene oxide-encapsulated α-Fe_2O_3 hybrid and its outstanding NO_2 gas sensing properties at room temperature, Sens. Actuators B Chem. 261 (2018) 252–263.
[16] B. Zhang, J. Liu, Enhanced gas sensing properties to acetone vapor achieved by α-Fe_2O_3 particles ameliorated with reduced graphene oxide sheets, Sens. Actuators B Chem. 241 (2017) 904–914.
[17] J. Liu, L. Shan, B. Zhang, Flower-like In_2O_3 modified by reduced graphene oxide sheets serving as a highly sensitive gas sensor for trace NO_2 detection, J. Colloid Interface Sci. 504 (2017) 206–213.
[18] J. Liu, L. Shan, B. Zhang, Ultrasensitive and low detection limit of nitrogen dioxide gas sensor based on flower-like ZnO hierarchical nanostructure modified by reduced graphene oxide, Sens. Actuators B Chem. 249 (2017) 715–724.
[19] D.J. Late, Y.K. Huang, B. Liu, Sensing behavior of atomically thin-layered MoS_2 transistors, ACS Nano 7 (2013) 4879–4891.
[20] A.N. Abbas, B. Liu, L. Chen, Y. Ma, Black phosphorus gas sensors, ACS Nano 9 (2015) 5618–5624.
[21] E. Lee, A. VahidMohammadi, B.C. Prorok, Room temperature gas sensing of two dimensional titanium carbide (Mxene), ACS Appl. Mater. Interfaces 9 (2017) 37184–37190.
[22] Q.H. Wang, K. Kalantar-Zadeh, Electronics and optoelectronics of two dimensional transition metal dichalcogenides, Nat. Nanotechnol. 7 (2012) 699–712.
[23] M. Chhowalla, H.S. Shin, G. Eda, L.J. Li, The chemistry of two-dimensional layered transition metal dichalcogenide nanosheets, Nat. Chem. 5 (2013) 263–275.
[24] J.A. Wilson, A.D. Yoffe, The transition metal dichalcogenides discussion and tnterpretation of the observed optical, electrical and structural properties, Adv. Phys. 18 (1969) 193–335.
[25] T.O. ehling, K.S. Novoselov, Molecular doping of graphene, Nano Lett. 8 (2008) 173–177.
[26] O. Leenaerts, B. Partoens, F.M. Peeters, Adsorption of H_2O, NH_3, CO, NO_2, and NO on graphene: a first-principles study, Phys. Rev. B: Condens. Matter Mater. Phys. 77 (2008) 125416.
[27] T. Hu, I.C. Gerber, Theoretical study of the interaction of electron donor and acceptor molecules with graphene, J. Phys. Chem. C 117 (2013) 2411–2420.
[28] C. Malagù, A. Giberti, S. Morandi, Electrical and spectroscopic analysis in nanostructured SnO_2: "long-term" resistance drift is due to in-diffusion, J. Appl. Phys. 110 (2011) 093711.
[29] C.M. Aldao, D.A. Mirabella, M.A. Ponce, A. Giberti, C. Malagù, Role of intragrain oxygen diffusion in polycrystalline tin oxide conductivity, J. Appl. Phys. 109 (2011) 063723.
[30] W. Deng, X. Chen, Z. Liu, A. Hu, Q. Tang, Z. Li, Y. Xiong, Three-dimensional structure-based tin disulfide/vertically aligned carbon nanotube arrays composites as high-performance anode materials for lithium ion batteries, J. Power Sources 277 (2015) 131–138.
[31] A. Giberti, A. Gaiardo, Tin (IV) sulfide nanorods as a new gas sensing material, Sens. Actuators B Chem. 223 (2016) 827–833.
[32] S.G. Patil, R.H. Tredgold, Electrical and photoconductive properties of SnS_2 crystals, J. Phys. D: Appl. Phys. 4 (1971) 718.
[33] S.H. El-Mahalawy, B.L. Evans, Temperature dependence of the electrical conductivity and hall coefficient in 2H-MoS_2, $MoSe_2$, WSe_2, and $MoTe_2$, Phys. Status Solidi B 79 (1977) 713–722.
[34] J.Z. Ou, W. Ge, B. Carey, T. Daeneke, Physisorption-based charge transfer in two-dimensional SnS_2 for selective and reversible NO_2 gas sensing, ACS Nano 9 (2015) 10313–10323.
[35] A. Dumbrava, C. Badea, G. Prodan, I. Popovici, V. Ciupina, Zinc sulfide fine particles obtained at low temperature, Chalcogenide Lett. 6 (2009) 437–443.
[36] Y.C. Zhang, Z.N. Du, K.W. Li, M. Zhang, Size-controlled hydrothermal synthesis of SnS2 nanoparticles with high performance in visible light-driven photocatalytic degradation of aqueous methyl orange, Sep. Purif. Technol. 81 (2011) 101–107.
[37] D.C. Marcano, D.V. Kosynkin, J.M. Berlin, A. Sinitskii, Z.Z. Sun, A. Slesarev, L.B. Alemany, W. Lu, J.M. Tour, Improved synthesis of graphene oxide, ACS Nano 4 (2010) 4806–4814.
[38] G. Su, V.G. Hadjiev, P.E. Loya, Chemical vapor deposition of thincrystals of layered semiconductor SnS_2 for fast photodetection application, Nano Lett. 15 (2015) 506–513.
[39] Z.Y. Qin, K. Xu, Enhanced room-temperature NH_3 gas sensing by 2D SnS_2 with sulfur vacancies synthesized by chemical exfoliation, Sens. Actuators B Chem. 262 (2018) 771–779.
[40] J.H. Ahn, M.J. Lee, H. Heo, J.H. Sung, K. Kim, H. Hwang, M.H. Jo, Deterministic two-dimensional polymorphism growth of hexagonal n-Type SnS(2) and orthorhombic p-Type SnS crystals, Nano Lett. 15 (2015) 3703–3708.
[41] H.S. Song, S.L. Li, L. Gao, Y. Xu, K. Ueno, J. Tang, Y.B. Cheng, K. Tsukagoshi, High-performance top-gated monolayer SnS_2 field-effect transistors and their integrated logic circuits, Nanoscale 5 (2013) 9666–9670.
[42] J. Zhang, L.H. Huang, Z.D. Lu, Z.L. Jin, X.Y. Wang, G.L. Xu, E.P. Zhang, H.B. Wang, Crystal face regulating MoS_2/TiO_2(001) heterostructures for high photocatalytic activity, J. Alloys Compd. 688 (2016) 840–848.
[43] Z.Y. Zhang, J.D. Huang, M.Y. Zhang, L. Yuan, B. Dong, Ultrathin hexagonal SnS_2 nanosheets coupled with g-C_3N_4 nanosheets as 2D/2D heterojunction photocatalysts toward high photocatalytic activity, Appl. Catal. B Environ. 163 (2015) 298–305.
[44] K. Zhou, W.J. Zhou, X.J. Liu, Y.H. Sang, S.Z. Ji, W. Li, J. Lu, L.G. Li, W.H. Niu, Ultrathin MoO_3 nanocrystals self-assembled on graphene nanosheets via oxygen bonding as supercapacitor electrodes of high capacitance and long cycle life, Nano Energy 12 (2015) 510–520.
[45] L. Dashairya, M. Sharma, SnS_2/RGO based nanocomposite for efficient photocatalytic degradation of toxic industrial dyes under visible-light irradiation, J. Alloys Compd. 774 (2019) 625–636.
[46] M.Y. Wang, Y. Huang, Y.D. Zhu, Binder-free flower-like SnS_2 nanoplates decorated on the graphene as a flexible anode for high-performance lithium-ion batteries, J. Alloys Compd. 774 (2019) 601–609.
[47] G. Zhao, J. Hou, Y.Z. Wu, Preparation of 2D MoS_2/graphene heterostructure through a monolayer intercalation method and its application as an optical modulator in pulsed laser generation, Adv. Optical Mater. 3 (2015) 937–942.
[48] R. Kumar, N. Goel, M. Kumar, UV-activated MoS_2 based fast and reversible NO_2 sensor at room temperature, ACS Sens. 2 (2017) 1744–1752.
[49] C. Zhang, M. Debliquy, H. Liao, Deposition and microstructure characterization of atmospheric plasma-sprayed ZnO coatings for NO_2detection, Appl. Surf. Sci. 256 (2010) 5905–5910.
[50] Z. Chen, J.R. Wang, D.X. Pan, Mimicking a dog's nose: scrolling graphene nanosheets, ACS Nano 12 (2018) 2521–2530.
[51] B. Cho, J. Yoon, S.K. Lim, A.R. Kim, Chemical sensing of 2D graphene/MoS_2 heterostructure device, ACS Appl. Mater. Interfaces 7 (2015) 16775–16780.
[52] W.J. Yan, Effects of ambient humidity and temperature on the NO_2 sensing characteristics of WS_2/graphene aerogel, Appl. Surface Sci. 450 (2018) 372–379.
[53] X. Geng, P.F. Lu, C. Zhang, Room temperature NO_2 gas sensors based on rGO@ ZnO_{1-x} composites: experiments and molecular dynamics simulation, Sens. Actuators B Chem. 282 (2019) 690–702.
[54] D. Gu, X. Li, Y. Zhao, Enhanced NO_2 sensing of SnO_2/SnS_2 heterojunction based sensor, Sens. Actuators B Chem. 244 (2017) 67–76.

Ming Cheng received his BE degree from Jilin University of China in 2017. He is currently working toward the MS degree in the Electronics Science and Engineering department, Jilin University. His current researches focus on the preparation and application of graphene and semiconductor oxide, especially in gas sensor.

Zepei Wu received his BE degree from Jilin University of China in 2017. Now he is studying for a MS degree in the Electronics Science and Engineering department, Jilin University. He is interested in the synthesis and application of graphene and semiconductor oxide, especially in gas sensor.

Guannan Liu received his BE degree from Jilin University of China in 2015. He is currently working toward the MS degree in the Electronics Science and Engineering department, Jilin University. His current researches focus on the synthesis of carbon dots and their applications.

Lianjing Zhao received her MS degree from Jilin University of China in 2013. She is currently working toward the Ph.D. degree in the Electronics Science and Engineering department, Jilin University. Her research interests mainly focus on the on the development of the functional nanomaterials for biosensors.

Yuan Gao received her PhD degree from Department of Analytical Chemistry at Jilin University in 2012. Now she is an associate professor in Jilin University, China. Her current researches focus on the preparation and application of graphene and semiconductor oxide, especially in gas sensor and biosensor.

Bo Zhang received the BE degree in College of Chemistry from Jilin University in 2013. He is currently working toward the Dr. Degree in College of Electronic Science and Engineering, Jilin University. His research interests include the synthesis of graphene and its applications in gas sensors.

Fangmeng Liu received his PhD degree in 2017 from College of Electronic Science and Engineering, Jilin University, China. Now he is a lecturer of Jilin University, China. His current research interests include the application of functional materials and development of solid state electrochemical gas sensor and flexible device.

Xu Yan received his M.S. degree in 2013 from Nanjing Agricultural University. He joined the group of Prof. Xingguang Su at Jilin University and received his Ph.D. degree in June 2017. Since then, he did postdoctoral work with Prof. Geyu Lu. Currently, his research interests mainly focus on the development of the functional nanomaterials for chem/bio sensors.

Xishuang Liang received the B. Eng. degree in Department of Electronic Science and Technology in 2004. He received his Doctor's degree in College of Electronic Science and Engineering at Jilin University in 2009. Now he is an associate professor of Jilin University, China. His current research is solid electrolyte gas sensor.

Peng Sun received his PhD degree from College of Electronic Science and Engineering, Jilin University, China in 2014. He was appointed the lecturer in Jilin University in the same year. Now, he is engaged in the synthesis and characterization of the semiconducting functional materials and gas sensors.

Geyu Lu received the B. Sci. degree in electronic sciences in 1985 and the M. Sci.degree in 1988 from Jilin University in China and the Dr. Eng. degree in 1998 from Kyushu University in Japan. Now he is a professor of Jilin University, China. His current research interests include the development of chemical sensors and the application of the function materials.